



# Global XCO<sub>2</sub> anomalies as seen by Orbiting Carbon Observatory-2

Janne Hakkarainen<sup>1</sup>, Iolanda Ialongo<sup>1</sup>, Shamil Maksyutov<sup>2</sup>, and David Crisp<sup>3</sup>

<sup>1</sup>Finnish Meteorological Institute, Helsinki, Finland

<sup>2</sup>Center for Global Environmental Research, National Institute for Environmental Studies, Tsukuba, Japan

<sup>3</sup>Jet Propulsion Laboratory/California Institute of Technology, Pasadena, CA, USA

**Correspondence:** Janne Hakkarainen ([janne.hakkarainen@fmi.fi](mailto:janne.hakkarainen@fmi.fi))

**Abstract.** NASA's carbon dioxide mission, Orbiting Carbon Observatory-2, has been operating for three full years (2015—2017). Here, we provide a global (60° S–60° N) view of the XCO<sub>2</sub> anomalies along with their annual variations and seasonal patterns. We show that the XCO<sub>2</sub> anomaly patterns are robust and consistent from year-to-year. We compare these anomalies to fluxes from anthropogenic, biospheric and biomass burning and to model-simulated local concentration enhancements.

5 We find that, despite the simplicity of the method, the anomalies describe the spatio-temporal variability of XCO<sub>2</sub> (including anthropogenic emissions and seasonal variability related to vegetation and biomass burning) consistently with more complex model-based approaches. We see, for example, that positive anomalies correspond to fossil fuel combustion over the major industrial areas (e.g., China, eastern USA, central Europe, India, and the Highveld region in South Africa), shown as large positive XCO<sub>2</sub> enhancements in the model simulations. Also, we find corresponding positive anomalies and fluxes over biomass burn-

10 ing areas during different fire seasons. On the other hand, the largest negative anomalies correspond to the growing season in the northern middle latitudes, characterized by negative XCO<sub>2</sub> enhancements from simulations and high SIF values (indicating the occurrence of photosynthesis). Finally, we show how XCO<sub>2</sub> anomalies facilitate the detection of anthropogenic signatures for several local scale case studies, both in the Northern and Southern Hemisphere. The results demonstrate the potential of satellite-based XCO<sub>2</sub> observations for understanding the role of man-made and natural contributions to the atmospheric CO<sub>2</sub>

15 levels.

*Copyright statement.*

## 1 Introduction

The first operational measurements of atmospheric carbon dioxide (CO<sub>2</sub>) were started at Mauna Loa Observatory in 1958 by Charles David Keeling. These measurements now form the iconic Keeling curve that shows, in addition to seasonal variations,

20 rapidly increasing levels of CO<sub>2</sub> in the atmosphere due to the burning of fossil fuels. Now, 60 years later, the measured levels of CO<sub>2</sub> are about 100 ppm higher than the original levels of about 315 ppm. Today, the atmospheric CO<sub>2</sub> concentration is measured all over the world. However, the measurement networks tend to be more dense in the Western world.



One of the most important applications of CO<sub>2</sub> measurements is to infer the surface CO<sub>2</sub> fluxes, i.e., sources and sinks (or emissions into and removal from the atmosphere). As the measurement networks tend to be unevenly distributed, one natural way to extend the spatial distribution is to use space-based observations of the column-averaged CO<sub>2</sub> dry air mole fraction, XCO<sub>2</sub>. The main advantage of space-based observations is that they provide global measurements of CO<sub>2</sub> obtained with the same measurement device. On the other hand, because XCO<sub>2</sub> is a vertically averaged quantity, it is less sensitive to the surface fluxes. Ideally, the inverse modeling systems that estimate CO<sub>2</sub> fluxes from atmospheric measurements, can assimilate measurements from all different types of sources.

One of the first instruments to measure greenhouse gases (GHGs) from space was SCIAMACHY (Scanning Imaging Absorption Spectrometer for Atmospheric Chartography), launched by the European Space Agency onboard the Envisat spacecraft in 2002 (Burrows et al., 1995). The first mission that provided XCO<sub>2</sub> measurements at a precision better than 0.6% is the Japanese GOSAT (Greenhouse Gases Observing Satellite), which has produced GHG measurements since April 2009 (Yokota et al., 2009). In 2014, NASA launched its CO<sub>2</sub> mission, the Orbiting Carbon Observatory-2 (OCO-2), which has been providing CO<sub>2</sub> measurements since September 2014 (Crisp et al., 2017; Eldering et al., 2017). An increasing number of CO<sub>2</sub> measuring satellites, including the Chinese TanSat (Yang et al., 2018; Cai et al., 2014), Fen-Yun-3D and Gaofen 5 have been launched since 2016 and other are being planned<sup>1</sup>.

Although the current space-based CO<sub>2</sub> missions were mainly driven by the need to better understand the biospheric carbon fluxes (Nassar et al., 2017), satellite-based CO<sub>2</sub> observations have been used also in anthropogenic CO<sub>2</sub> studies. For example, Reuter et al. (2014) analyzed the CO<sub>2</sub>-to-NO<sub>2</sub> emission ratios with collocated SCIAMACHY data, Janardanan et al. (2016) studied localized CO<sub>2</sub> enhancements using GOSAT data, Kort et al. (2012) studied the CO<sub>2</sub> signal from Los Angeles and Mumbai megacities from GOSAT data, Nassar et al. (2017) estimated the CO<sub>2</sub> emissions from individual power plants from OCO-2 data, Schwandner et al. (2017) analyzed localized carbon dioxide sources (e.g., Los Angeles) using OCO-2 data, and Ye et al. (2017) evaluated the possibility to constrain the fossil fuel CO<sub>2</sub> emissions from urban areas using OCO-2 observations. Since the Paris Agreement in 2015, the focus has shifted more and more on anthropogenic CO<sub>2</sub> research, and for example, the European Space Agency is currently planning a dedicated anthropogenic CO<sub>2</sub> monitoring mission.

Direct methods, i.e. the methods that do not involve atmospheric inverse modeling, have been recently developed to study anthropogenic CO<sub>2</sub> emissions. These methods can be divided in two categories a) methods that study anthropogenic sources from individual orbits (e.g., Nassar et al., 2017; Schwandner et al., 2017); and b) methods that average data from long periods of time (e.g., Hakkarainen et al., 2016). One large obstacle limiting the quantification of anthropogenic CO<sub>2</sub> flux from space, is the limited mapping capability of current satellite missions. GOSAT provides single soundings with 10.5 km diameter resolution that are separated by ~250 km. OCO-2 provides measurements with eight 2.25 km long footprints along a narrow (0.4 to 1.29 km) swath, but the swaths are separated by ~1.5 degrees of longitude. In both cases the data coverage is quite sparse. Figure 1 illustrates an example of the OCO-2 measurement locations during different periods of time: one day, one week, one month and one year. In addition to the nominal measurements, special target mode measurements are performed in selected measurement locations for anthropogenic and/or validation purposes (Wunch et al., 2017).

<sup>1</sup>See, e.g., [https://en.wikipedia.org/wiki/Space-based\\_measurements\\_of\\_carbon\\_dioxide](https://en.wikipedia.org/wiki/Space-based_measurements_of_carbon_dioxide)



The aim of this paper is to extend the results presented in (Hakkarainen et al., 2016), and provide global (60° S–60° N) view on XCO<sub>2</sub> anomalies as seen by OCO-2 for three full years 2015–2017. In Section 2 we introduce the data sets and methods to derive XCO<sub>2</sub> anomalies. In Section 3, we analyse the annual and seasonal patterns of XCO<sub>2</sub> anomalies, and we discuss them in terms of anthropogenic, biospheric and biomass burning contributions. Finally, Section 4 concludes the paper.

## 5 2 Materials and Methods

### 2.1 OCO-2 data

We use data from NASA's OCO-2 satellite (Crisp et al., 2017). The satellite was launched on 2 July 2014, and now leads the 705 km Afternoon Constellation (also known as the A-Train). OCO-2 has provided science data since September 2014.

The instrument measures the backscattered solar light in three spectral regions: oxygen A-band at 0.765 microns and CO<sub>2</sub> bands at 1.61 and 2.06 microns. It provides data with eight 2.25 km long footprints along a narrow (0.4 to 1.29 km) swath. The retrieved quantity is column-averaged dry air mole fraction of CO<sub>2</sub>, XCO<sub>2</sub>.

In this paper, we use the latest OCO-2 data version (V8r) available from the MIRADOR platform at <http://mirador.gsfc.nasa.gov>. We use the lite files that include bias correction and data screening. We only use the data points where the quality flags are set to zero. The validation of OCO-2 data against results from the Total Carbon Column Observing Network (TCCON) indicates that the absolute median differences are less than 0.4 ppm and the RMS differences are less than 1.5 ppm. The bias appears to depend on latitude, surface properties, and scattering by aerosols (Wunch et al., 2017).

### 2.2 XCO<sub>2</sub> anomalies

Because of the long lifetime of CO<sub>2</sub> in the atmosphere, it is intrinsically difficult to derive information about the spatial distribution of CO<sub>2</sub> emission areas from satellite measurements of CO<sub>2</sub> concentrations. CO<sub>2</sub> accumulates in the atmosphere with a growth rate of about 2–3 ppm per year. The overall background level is currently in the order of 400 ppm. Therefore, the approach used to map short-lived air pollutants, like nitrogen dioxide (NO<sub>2</sub>), based on averaging out the outflow downwind from the emission sources, cannot be directly applied to space-based CO<sub>2</sub> measurements. The large CO<sub>2</sub> background and seasonal variability must be removed before being able to highlight the emission areas.

In order to extract information about the anthropogenic signatures from OCO-2 retrievals, we use the concept of XCO<sub>2</sub> anomaly (Hakkarainen et al., 2016), defined as the difference between the individual XCO<sub>2</sub> value measured by OCO-2 and the background (i.e., the daily median XCO<sub>2</sub> over a certain area):

$$\text{XCO}_2(\text{anomaly}) = \text{XCO}_2(\text{individual}) - \text{XCO}_2(\text{daily median}). \quad (1)$$

This equation provides an anomaly value for each OCO-2 data point. Figure 1 shows a scatter plot of these XCO<sub>2</sub> anomalies for one day, one week, one month and one year. Using the daily median as background allows us to remove the seasonal



variability and the increasing trend of CO<sub>2</sub> concentrations. Once we obtain the anomalies for each OCO-2 measurement point, we define a spatial grid (e.g., 1° × 1°, latitude-longitude) and calculate the mean at each grid point over a defined period of time. This average essentially removes the effect of the different wind patterns and the resulting anomaly maps illustrate the areas where CO<sub>2</sub> is emitted (positive anomalies) into the atmosphere and those acting as sinks, where CO<sub>2</sub> is absorbed at the surface (negative anomalies). The strength of this approach is that it only uses satellite-based measurements and is not dependent on patterns in *a priori* fields, external data or other assumptions in atmospheric chemistry-transport models.

One question is how do we define the area over which we calculate the daily median. In Hakkarainen et al. (2016), we focused on three large anthropogenic emission areas: 1) North America, 2) Europe, northern Africa and Middle East, and 3) East Asia. In this paper, we use the Northern and Southern hemisphere (60° S–0° S and 0° N–60° N) over land as background areas, because we aim to obtain comparable anomalies for different regions. Thus, we assume the hemispherical background (median) as representative of the seasonal variability at different latitudes. In Section 3.3, we discuss how the choice of the background area (e.g., different latitude bands) affects the calculation of the XCO<sub>2</sub> anomalies.

Another issue is related to the number of satellite measurements available for the calculation of the anomalies over different regions and seasons. A lack of data is expected, for example, over areas frequently covered by clouds or with a large aerosol load, as well as at middle-latitudes in autumn-winter when the Sun is too low for a successful XCO<sub>2</sub> retrieval. In Section 3, we analyze the effect of the inhomogeneous distribution of OCO-2 data on the anomaly's spatio-temporal patterns.

## 2.3 Auxiliary datasets

### 2.3.1 CarbonTracker CO<sub>2</sub> fluxes

In order to better understand the spatio-temporal patterns in the XCO<sub>2</sub> anomaly distribution, we analyze the NOAA CarbonTracker (CT2016; Peters et al., 2007) flux maps<sup>2</sup>. In particular, we consider the biospheric fluxes as well as those associated with biomass burning emissions. As input information, CT2016 uses Global Fire Emissions Database (GFED) 4.1. that is based on MODIS (Moderate Resolution Imaging Spectroradiometer) observations of fire counts. The *a priori* biospheric fluxes are based on the Carnegie-Ames Stanford Approach (CASA) biogeochemical model, and their scaling factors are estimated using CT2016.

### 2.3.2 Solar-induced chlorophyll fluorescence (SIF)

We analyze solar-induced chlorophyll fluorescence (SIF) also measured by the OCO-2 instrument (Frankenberg et al., 2014) at 757 nm and 772 nm. Here, we use the 757 nm data. SIF can be seen as a proxy for the vegetation gross primary production (GPP) (Sun et al., 2017), defined as the synthesis of organic compounds from atmospheric CO<sub>2</sub> and principally occurring through the process of photosynthesis. Therefore, SIF data are expected to provide information on the effect of vegetation in the distribution of the XCO<sub>2</sub> anomalies and to complement their patterns.

<sup>2</sup>See also <https://www.esrl.noaa.gov/gmd/ccgg/carbontracker/fluxes.php>



### 2.3.3 XCO<sub>2</sub> enhancements from FLEXPART model

We use the Lagrangian particle dispersion model FLEXPART (FLEXible PARTicle dispersion model) (Stohl et al., 2005) to simulate anthropogenic and biospheric XCO<sub>2</sub> enhancements at OCO-2 measurements locations. We follow the approach used by Janardanan et al. (2016), where the localized GOSAT CO<sub>2</sub> enhancements are compared to the inventory-based CO<sub>2</sub> estimates using the FLEXPART model outputs. As there are about 85 000 OCO-2 data points per day, for computational reasons we aggregate an average OCO-2 data points to one-second ( $\leq 24$  soundings) averages, taken separately for OCO-2 footprints 1–4 and 5–8.

As input information for anthropogenic emissions, we use the high-resolution ODIAC (Open-Data Inventory for Anthropogenic Carbon dioxide) data set (Oda et al., 2018). In the ODIAC data set the anthropogenic CO<sub>2</sub> emissions are estimated in 1 km × 1 km resolution given the power plant emissions (intensity and geographical location) and satellite-observed nightlights. In the FLEXPART model simulations, from each aggregated OCO-2 data point, ten thousand virtual particles are released and transported three days backward in time with the three-dimensional wind field using parameterizations for turbulence and convection.

## 3 Results

### 3.1 Annual XCO<sub>2</sub> anomalies

Figure 2 illustrates the three-year average and the mean annual XCO<sub>2</sub> anomalies for the years 2015–2017. We observe that the largest anomalies correspond to the anthropogenic emission areas in China, North-East India, Middle East, central Europe, and eastern USA, as noted also in (Hakkarainen et al., 2016). In the Southern Hemisphere, the largest anthropogenic emission area, the Highveld region in South Africa, is clearly visible from the map. In the Northern Hemisphere, some smaller emission areas (e.g., Mexico City) can be identified also at global scale.

High positive XCO<sub>2</sub> anomalies can be observed also where anthropogenic emissions from fossil fuels are not expected. For example in northern and southern Africa, Indonesia, Indochina, and South America we see large emission areas. These mostly correspond to large-scale biomass burning, and also to positive biospheric fluxes.

The largest negative anomalies are observed in the northern middle-latitudes (40° N–60° N). These are clearly connected to the strong biospheric sink during the growing season. We note that this area is mainly sampled by OCO-2 during summer months and not during winter (when there is not enough sunlight to take the measurement). This produces particularly low negative anomalies in the annual anomaly maps. We also observe a large area with negative anomalies in the Southern Cone in South America.

The overall patterns observed in the annual maps are similar every year, i.e., the large areas with positive and negative anomalies are quite consistent. Also smaller areas with large anomalies seem to be consistently visible in the different years (e.g., the Highveld region). Some differences in the XCO<sub>2</sub> anomaly patterns between different years are, at least partly, related to the sampling of the instrument and the number of data points available. These are most visible for example at northern mid-



latitudes where we can still identify the “satellite tracks” from the map. In the Figure S1 of the supplementary material, we present the maps of the number of data points that was used to calculate the mean in Fig. 2. In addition to northern latitudes, the number of data points is also lower in places with high cloud density and/or large aerosol load (Himalaya, Amazonia, central Africa and China).

### 5 3.2 Seasonal XCO<sub>2</sub> anomalies

Figure 3 illustrates the mean seasonal XCO<sub>2</sub> anomalies calculated from the period September 2014 to December 2017. The different seasons are defined as September-October-November (SON), December-January-February (DJF), March-April-May (MAM) and June-July-August (JJA). The large-scale patterns on SON, DJF, MAM look very similar to each other and to the annual mean, while in JJA the anomaly distribution looks quite different, with strong negative anomalies over the Northern Hemispheric mid-latitudes and relatively high anomalies over the whole tropical latitudinal band. The negative anomalies are larger than those obtained for SON and MAM. No OCO-2 observations are available during winter months (DJF) over the northern mid-latitudes.

In order to understand this seasonal variability, we analyze the seasonal distribution of the solar-induced chlorophyll fluorescence (SIF, Fig. 4), also measured by OCO-2, as well as the fluxes from the NOAA CarbonTracker model (Fig. 5). Both SIF and CT flux spatial distribution show how the negative anomalies observed during JJA are related to the biospheric sink (i.e., high SIF and negative fluxes).

When comparing the XCO<sub>2</sub> anomaly patterns in Africa in different seasons, we find the largest anomalies in the northern biomass burning area during winter months (DJF) and relatively smaller anomalies during SON and MAM. During summer months, we find mainly negative anomalies over the same area. These features correspond directly to those we observe in the flux maps, i.e., strong emissions from biomass burning during winter and sink during summer (Fig. 5, right column). SIF is also higher during summer months, when anomalies are negative. Also, in the southern biomass burning area in Africa, we observe the largest anomalies during JJA, when the biomass burning emissions are the strongest (Fig. 5, right column) and SIF values relatively small. The largest negative anomalies are on DJF, when there are very little emissions from biomass burning. From the anomaly maps (Fig. 3) we find that the anomalies over the Highveld industrial area in South Africa are the largest during JJA and SON, when the draw-down effect is minimum.

When looking at XCO<sub>2</sub> anomalies in South America, one evident problem is related to the number of data points available over Amazonia. The XCO<sub>2</sub> anomaly values seem to be positive throughout the year, although, the SIF is also positive. Signatures from biomass burning and positive biospheric fluxes are visible also in the anomalies during SON. In the Southern Cone, the anomalies are most negative during SON and DJF, which is in line with the SIF and biospheric flux maps.

In Indochina, the anomalies are positive throughout the year. From the biospheric flux maps we would expect positive fluxes during MAM and JJA. On the other hand, the largest SIF values are observed during JJA. During DJF and MAM we, see the signature of strong emission from fires in the anomalies and flux maps (Fig. 5, right column). We would expect however to see negative anomalies during SON due to the strong biospheric sink, but we find only slightly smaller positive anomalies. In the Indian peninsula during SON and DJF we see negative anomalies in the southern part of India where we would expect to



see signs of anthropogenic emissions. These correspond to biospheric sink that we see in the flux map. During MAM, we find positive  $XCO_2$  anomalies as expected from anthropogenic emissions when the biospheric flux is low.

Interesting seasonal patterns can be observed when looking at the largest anthropogenic emission areas, i.e., China, central Europe and eastern USA. For example China and central Europe show positive anomalies during all seasons, and eastern USA in all seasons but JJA (when there is very strong biospheric sink). Also, positive anomalies in China and central Europe are lower during JJA. All three areas have largest anomalies during DJF when also the biospheric flux is positive.

### 3.3 Latitudinal effects

When calculating the  $XCO_2$  anomaly, one critical point is how we define the background region from which we obtain the daily median in Eq. 1. Figure 6 illustrates the daily median  $XCO_2$  time series calculated from different latitude bands (every 20° in latitude in the range 60° S–60° S). We observe that the hemispheric (0° N–60° N and 60° S–0° S) seasonal cycles (black lines in Fig. 6) are clearly different from each others and we cannot use the same background areas (i.e., median values) for the Northern and Southern hemisphere.

In the Southern Hemisphere, the seasonal cycles are very similar for all 20-degree latitude bands. The hemispheric (60° S–0° S) daily median provides a stable estimate of the background, which is mostly driven by the 40° S–20° S seasonal cycle in the terrestrial biosphere. In the Northern Hemisphere, the seasonal cycle is more variable in different latitude bands. In particular, the seasonal cycle for the 40° N–60° N latitude band shows higher daily medians compared to the hemispheric values during winter months and much smaller values during spring and summer months, due to the strong biospheric sink in the Northern Hemisphere. The hemispheric (0° N–60° N) daily median is usually closer to the 0° N–20° N and 20° N–40° N seasonal cycles, however, it becomes closer to those from the 40° N–60° N latitude band during summer months, when more observations are available from this area.

Figure S2 in the supplementary material illustrates how the seasonal  $XCO_2$  anomalies would change if calculated using the 20-degree latitude bands as background. When comparing to Fig. 3, we observe very similar patterns except for the Northern Hemispheric summer months. During JJA, we notice the sharp change in the background at 40° N and less strong negative anomalies for the 40° N–60° N latitude band, because of the smaller daily median values. Vice versa, the positive anomalies that we see on Europe and western North America are now stronger. For the 0° N–40° N latitude band, we find that the anomalies are generally lower and closer to those from the other seasons. In particular, the strong positive anomalies that we observed in Northern and Central America are not evident anymore.

### 3.4 Modeling results

In this section, we analyze the  $XCO_2$  enhancements related to fossil fuel combustion and biospheric fluxes corresponding to the OCO-2 pixels using the Lagrangian FLEXPART model. This allows us to account for the effect of OCO-2 sampling and transport by the wind. Figure 7 illustrates the modeled  $XCO_2$  enhancements for the year 2015 (the results for year 2016 are shown in Fig. S3 in the supplementary material). We illustrate the contribution from the ODIAC fossil fuel fluxes alone (Fig. 7, upper panel) and together with the biospheric contribution (Fig. 7, lower panel). The anthropogenic component shows



spatial patterns very similar to those observed from the XCO<sub>2</sub> anomalies in Fig. 2, with the three region with high positive enhancements in eastern USA, Europe and China. In the Southern Hemisphere, the Highveld region in South Africa shows the strongest anthropogenic signal, together for example with the area around Sidney in Australia. When adding the biospheric component, we also find negative values in northern mid-latitudes and in the Southern Cone in South America, as observed  
5 from the anomalies in Fig. 2. In Europe, the large anthropogenic XCO<sub>2</sub> enhancements are drawn down by the biospheric sink (Fig. 7 - lower panel).

Figure 8 illustrates the results of the FLEXPART seasonal simulations. We find that the Highveld region is clearly visible during SON and JJA, while it is not detectable anymore during DJF due to effect of the biospheric sink. The same feature is also visible in the seasonal anomalies in Fig 3. There are also differences between seasonal FLEXPART model simulations  
10 and OCO-2 XCO<sub>2</sub> anomalies, particularly during JJA when the anomalies show a strong latitudinal gradient as discussed in Section 3.3.

Finally, four local “case studies” for both FLEXPART enhancements and OCO-2 anomalies are illustrated in Fig. 9. The first one is the Iberian peninsula, where OCO-2 XCO<sub>2</sub> retrievals are available consistently throughout the year. We can clearly observe the positive signal from different cities over the coastal areas in the XCO<sub>2</sub> anomalies. The second one is the already  
15 mentioned Highveld industrial region in South Africa. In this case, the anthropogenic signatures seem more localized in the FLEXPART simulations than in the anomaly maps, although positive anomalies are clearly visible over the area as well. The third case study is India, where we can see clear positive signal in both OCO-2 and FLEXPART data, with some discrepancies in the exact location of the anthropogenic signatures. The last case is Mexico City where we also see strong anthropogenic signatures (i.e., positive enhancements and anomalies), related to the emissions from the city as well as power plants in the  
20 area.

In the supplementary material (Figs. S4–S8) we also illustrate similar case studies for the largest anthropogenic emission areas.

#### 4 Summary and remarks

In this paper, we analyzed the global (60° S–60° N) XCO<sub>2</sub> anomalies for three full years 2015–2017. We describe the large-  
25 scale features like the main anthropogenic emission areas, biomass burning regions, and biospheric sinks. We also see that the patterns observed in OCO-2 annual XCO<sub>2</sub> anomalies are robust and consistent from year-to-year. The OCO-2 data were also used to study the seasonal XCO<sub>2</sub> anomalies. From the seasonal XCO<sub>2</sub> anomalies we can identify the patterns in the Northern Hemispheric growing season and also the different fire seasons in Africa. In addition to large-scale features, we also visualize different local “case studies” with high anomalies associated with anthropogenic emissions in both the Northern and Southern  
30 Hemispheres. These examples highlight the potential of space-based data for further local studies.

The method proposed in this paper, i.e the hemispheric XCO<sub>2</sub> anomalies, is quite different from many other approaches where satellite CO<sub>2</sub> data are used. In GHG research, inverse modeling is often used for estimating surface fluxes from atmospheric measurements. Traditionally, this approach was designed for surface CO<sub>2</sub> measurements, and most inverse modeling



algorithms do not yet utilize the space-based data in their fullest potential. For example, in such applications, chemistry transport models still use spatial resolutions much lower than what OCO-2 is providing. In addition, typically, only the scaling factors for *a priori* biospheric fluxes are estimated, and the sub-regional patterns seen in the flux maps come from external modeling. Often the emissions from fossil fuel combustion and biomass burning are also imposed and not estimated. The approach taken here, is free from atmospheric modeling and *a priori* fluxes, and all of the features seen in the XCO<sub>2</sub> anomaly maps come from satellite data alone. On the other hand, instrument sampling, background choice and bias correction do have an impact on the OCO-2 XCO<sub>2</sub> anomaly patterns.

The anomaly approach used here is very attractive for several reasons (e.g., simplicity, robustness and model-free), but it also includes some challenges. One peculiar feature of the approach is that we calculate anomaly with respect to a certain background. Thus, we have to define the background area from which we calculate the daily median from. We showed that the approach is not too sensitive to these assumptions and that hemispheric anomalies provide robust tool for global analysis. An exception is the Northern Hemispheric summer months, when we have the strong biospheric sink that define the CO<sub>2</sub> seasonal cycle and OCO-2 measurements are only scarcely available during the other seasons. When studying local case studies on regional scale, a different background region could be selected. Another feature of the anomaly approach is that the XCO<sub>2</sub> anomalies (given in ppms) are not directly convertible to fluxes (given in ktons). The approach often taken with short-lived air pollutants is to use a statistical model that describes their spatial distribution near the emission sources as a function of wind speed and direction (e.g., Beirle et al., 2011; Fioletov et al., 2016). In the future, a similar approach might also be possible with XCO<sub>2</sub> anomalies, for example using CO<sub>2</sub> measuring satellites with wider swaths, such as the anthropogenic CO<sub>2</sub> monitoring mission planned by the European Space Agency.

*Data availability.* OCO-2 data can be downloaded using the MIRADOR platform (<http://mirador.gsfc.nasa.gov>). NOAA CarbonTracker CT2016 data is available from <http://carbontracker.noaa.gov>. ODIAC fossil fuel CO<sub>2</sub> emissions dataset is available from <http://db.cger.nies.go.jp/dataset/ODIAC/>. FLEXPART model simulation can be obtained from Shamil Maksyutov ([shamil@nies.go.jp](mailto:shamil@nies.go.jp)).

*Competing interests.* The authors declare that they have no competing interests.

*Acknowledgements.* Janne Hakkarainen and Iolanda Ialongo acknowledge the funding from the Academy of Finland, project numbers 312125 and 303876, respectively. Shamil Maksyutov is supported by the GOSAT project. Part of the research described in this paper was carried out at the Jet Propulsion Laboratory, California Institute of Technology, under a contract with the National Aeronautics and Space Administration.



## References

- Beirle, S., Boersma, K. F., Platt, U., Lawrence, M. G., and Wagner, T.: Megacity Emissions and Lifetimes of Nitrogen Oxides Probed from Space, *Science*, 333, 1737–1739, <https://doi.org/10.1126/science.1207824>, <http://science.sciencemag.org/content/333/6050/1737>, 2011.
- Burrows, J., Hölzle, E., Goede, A., Visser, H., and Fricke, W.: SCIAMACHY—scanning imaging absorption spectrometer for atmospheric chartography, *Acta Astronautica*, 35, 445–451, [https://doi.org/https://doi.org/10.1016/0094-5765\(94\)00278-T](https://doi.org/https://doi.org/10.1016/0094-5765(94)00278-T), <http://www.sciencedirect.com/science/article/pii/009457659400278T>, earth Observation, 1995.
- Cai, Z., Liu, Y., and Yang, D.: Analysis of XCO<sub>2</sub> retrieval sensitivity using simulated Chinese Carbon Satellite (TanSat) measurements, *Science China Earth Sciences*, 57, 1919–1928, <https://doi.org/10.1007/s11430-013-4707-1>, <https://doi.org/10.1007/s11430-013-4707-1>, 2014.
- 10 Crisp, D., Pollock, H. R., Rosenberg, R., Chapsky, L., Lee, R. A. M., Oyafuso, F. A., Frankenberg, C., O'Dell, C. W., Bruegge, C. J., Doran, G. B., Eldering, A., Fisher, B. M., Fu, D., Gunson, M. R., Mandrake, L., Osterman, G. B., Schwandner, F. M., Sun, K., Taylor, T. E., Wennberg, P. O., and Wunch, D.: The on-orbit performance of the Orbiting Carbon Observatory-2 (OCO-2) instrument and its radiometrically calibrated products, *Atmospheric Measurement Techniques*, 10, 59–81, <https://doi.org/10.5194/amt-10-59-2017>, <https://www.atmos-meas-tech.net/10/59/2017/>, 2017.
- 15 Eldering, A., Wennberg, P. O., Crisp, D., Schimel, D. S., Gunson, M. R., Chatterjee, A., Liu, J., Schwandner, F. M., Sun, Y., O'Dell, C. W., Frankenberg, C., Taylor, T., Fisher, B., Osterman, G. B., Wunch, D., Hakkarainen, J., Tamminen, J., and Weir, B.: The Orbiting Carbon Observatory-2 early science investigations of regional carbon dioxide fluxes, *Science*, 358, <https://doi.org/10.1126/science.aam5745>, <http://science.sciencemag.org/content/358/6360/eaam5745>, 2017.
- Fioletov, V. E., McLinden, C. A., Krotkov, N., Li, C., Joiner, J., Theys, N., Carn, S., and Moran, M. D.: A global catalogue of large SO<sub>2</sub> sources and emissions derived from the Ozone Monitoring Instrument, *Atmospheric Chemistry and Physics*, 16, 11 497–11 519, <https://doi.org/10.5194/acp-16-11497-2016>, <https://www.atmos-chem-phys.net/16/11497/2016/>, 2016.
- Frankenberg, C., O'Dell, C., Berry, J., Guanter, L., Joiner, J., Köhler, P., Pollock, R., and Taylor, T. E.: Prospects for chlorophyll fluorescence remote sensing from the Orbiting Carbon Observatory-2, *Remote Sensing of Environment*, 147, 1 – 12, <https://doi.org/https://doi.org/10.1016/j.rse.2014.02.007>, <http://www.sciencedirect.com/science/article/pii/S0034425714000522>, 2014.
- 25 Hakkarainen, J., Ialongo, I., and Tamminen, J.: Direct space-based observations of anthropogenic CO<sub>2</sub> emission areas from OCO-2, *Geophysical Research Letters*, 43, 11,400–11,406, <https://doi.org/10.1002/2016GL070885>, <https://agupubs.onlinelibrary.wiley.com/doi/abs/10.1002/2016GL070885>, 2016.
- Janardanan, R., Maksyutov, S., Oda, T., Saito, M., Kaiser, J. W., Ganshin, A., Stohl, A., Matsunaga, T., Yoshida, Y., and Yokota, T.: Comparing GOSAT observations of localized CO<sub>2</sub> enhancements by large emitters with inventory-based estimates, *Geophysical Research Letters*, 30, 3486–3493, <https://doi.org/10.1002/2016GL067843>, <https://agupubs.onlinelibrary.wiley.com/doi/abs/10.1002/2016GL067843>, 2016.
- Kort, E. A., Frankenberg, C., Miller, C. E., and Oda, T.: Space-based observations of megacity carbon dioxide, *Geophysical Research Letters*, 39, <https://doi.org/10.1029/2012GL052738>, <https://agupubs.onlinelibrary.wiley.com/doi/abs/10.1029/2012GL052738>, 2012.
- Nassar, R., Hill, T. G., McLinden, C. A., Wunch, D., Jones, D. B. A., and Crisp, D.: Quantifying CO<sub>2</sub> Emissions From Individual Power Plants From Space, *Geophysical Research Letters*, 44, 10,045–10,053, <https://doi.org/10.1002/2017GL074702>, <https://agupubs.onlinelibrary.wiley.com/doi/abs/10.1002/2017GL074702>, 2017.
- 35



- Oda, T., Maksyutov, S., and Andres, R. J.: The Open-source Data Inventory for Anthropogenic CO<sub>2</sub>, version 2016 (ODIAC2016): a global monthly fossil fuel CO<sub>2</sub> gridded emissions data product for tracer transport simulations and surface flux inversions, *Earth System Science Data*, 10, 87–107, <https://doi.org/10.5194/essd-10-87-2018>, <https://www.earth-syst-sci-data.net/10/87/2018/>, 2018.
- Peters, W., Jacobson, A. R., Sweeney, C., Andrews, A. E., Conway, T. J., Masarie, K., Miller, J. B., Bruhwiler, L. M. P., Pétron, G., Hirsch, A. I., Worthy, D. E. J., van der Werf, G. R., Randerson, J. T., Wennberg, P. O., Krol, M. C., and Tans, P. P.: An atmospheric perspective on North American carbon dioxide exchange: CarbonTracker, *Proceedings of the National Academy of Sciences*, 104, 18 925–18 930, <https://doi.org/10.1073/pnas.0708986104>, <http://www.pnas.org/content/104/48/18925>, 2007.
- Reuter, M., Buchwitz, M., Hilboll, A., Richter, A., Schneising, O., Hilker, M., Heymann, J., Bovensmann, H., and Burrows, J. P.: Decreasing emissions of NO<sub>x</sub> relative to CO<sub>2</sub> in East Asia inferred from satellite observations, *Nature Geoscience*, 7, 792 EP –, <https://doi.org/10.1038/ngeo2257>, <http://dx.doi.org/10.1038/ngeo2257>, 2014.
- Schwandner, F. M., Gunson, M. R., Miller, C. E., Carn, S. A., Eldering, A., Krings, T., Verhulst, K. R., Schimel, D. S., Nguyen, H. M., Crisp, D., O'Dell, C. W., Osterman, G. B., Iraci, L. T., and Podolske, J. R.: Spaceborne detection of localized carbon dioxide sources, *Science*, 358, <https://doi.org/10.1126/science.aam5782>, <http://science.sciencemag.org/content/358/6360/eaam5782>, 2017.
- Stohl, A., Forster, C., Frank, A., Seibert, P., and Wotawa, G.: Technical note: The Lagrangian particle dispersion model FLEXPART version 6.2, *Atmospheric Chemistry and Physics*, 5, 2461–2474, <https://doi.org/10.5194/acp-5-2461-2005>, <https://www.atmos-chem-phys.net/5/2461/2005/>, 2005.
- Sun, Y., Frankenberg, C., Wood, J. D., Schimel, D. S., Jung, M., Guanter, L., Drewry, D. T., Verma, M., Porcar-Castell, A., Griffis, T. J., Gu, L., Magney, T. S., Köhler, P., Evans, B., and Yuen, K.: OCO-2 advances photosynthesis observation from space via solar-induced chlorophyll fluorescence, *Science*, 358, <https://doi.org/10.1126/science.aam5747>, <http://science.sciencemag.org/content/358/6360/eaam5747>, 2017.
- Wunch, D., Wennberg, P. O., Osterman, G., Fisher, B., Naylor, B., Roehl, C. M., O'Dell, C., Mandrake, L., Viatte, C., Kiel, M., Griffith, D. W. T., Deutscher, N. M., Velasco, V. A., Notholt, J., Warneke, T., Petri, C., De Maziere, M., Sha, M. K., Sussmann, R., Rettinger, M., Pollard, D., Robinson, J., Morino, I., Uchino, O., Hase, F., Blumenstock, T., Feist, D. G., Arnold, S. G., Strong, K., Mendonca, J., Kivi, R., Heikkinen, P., Iraci, L., Podolske, J., Hillyard, P. W., Kawakami, S., Dubey, M. K., Parker, H. A., Sepulveda, E., García, O. E., Te, Y., Jeseck, P., Gunson, M. R., Crisp, D., and Eldering, A.: Comparisons of the Orbiting Carbon Observatory-2 (OCO-2) X<sub>CO<sub>2</sub></sub> measurements with TCCON, *Atmospheric Measurement Techniques*, 10, 2209–2238, <https://doi.org/10.5194/amt-10-2209-2017>, <https://www.atmos-meas-tech.net/10/2209/2017/>, 2017.
- Yang, D., Liu, Y., Cai, Z., Chen, X., Yao, L., and Lu, D.: First Global Carbon Dioxide Maps Produced from TanSat Measurements, *Advances in Atmospheric Sciences*, 35, 621–623, <https://doi.org/10.1007/s00376-018-7312-6>, <https://doi.org/10.1007/s00376-018-7312-6>, 2018.
- Ye, X., Lauvaux, T., Kort, E. A., Oda, T., Feng, S., Lin, J. C., Yang, E., and Wu, D.: Constraining fossil fuel CO<sub>2</sub> emissions from urban area using OCO-2 observations of total column CO<sub>2</sub>, *Atmospheric Chemistry and Physics Discussions*, 2017, 1–30, <https://doi.org/10.5194/acp-2017-1022>, <https://www.atmos-chem-phys-discuss.net/acp-2017-1022/>, 2017.
- Yokota, T., Yoshida, Y., Eguchi, N., Ota, Y., Tanaka, T., Watanabe, H., and Maksyutov, S.: Global Concentrations of CO<sub>2</sub> and CH<sub>4</sub> Retrieved from GOSAT: First Preliminary Results, *SOLA*, 5, 160–163, <https://doi.org/10.2151/sola.2009-041>, 2009.

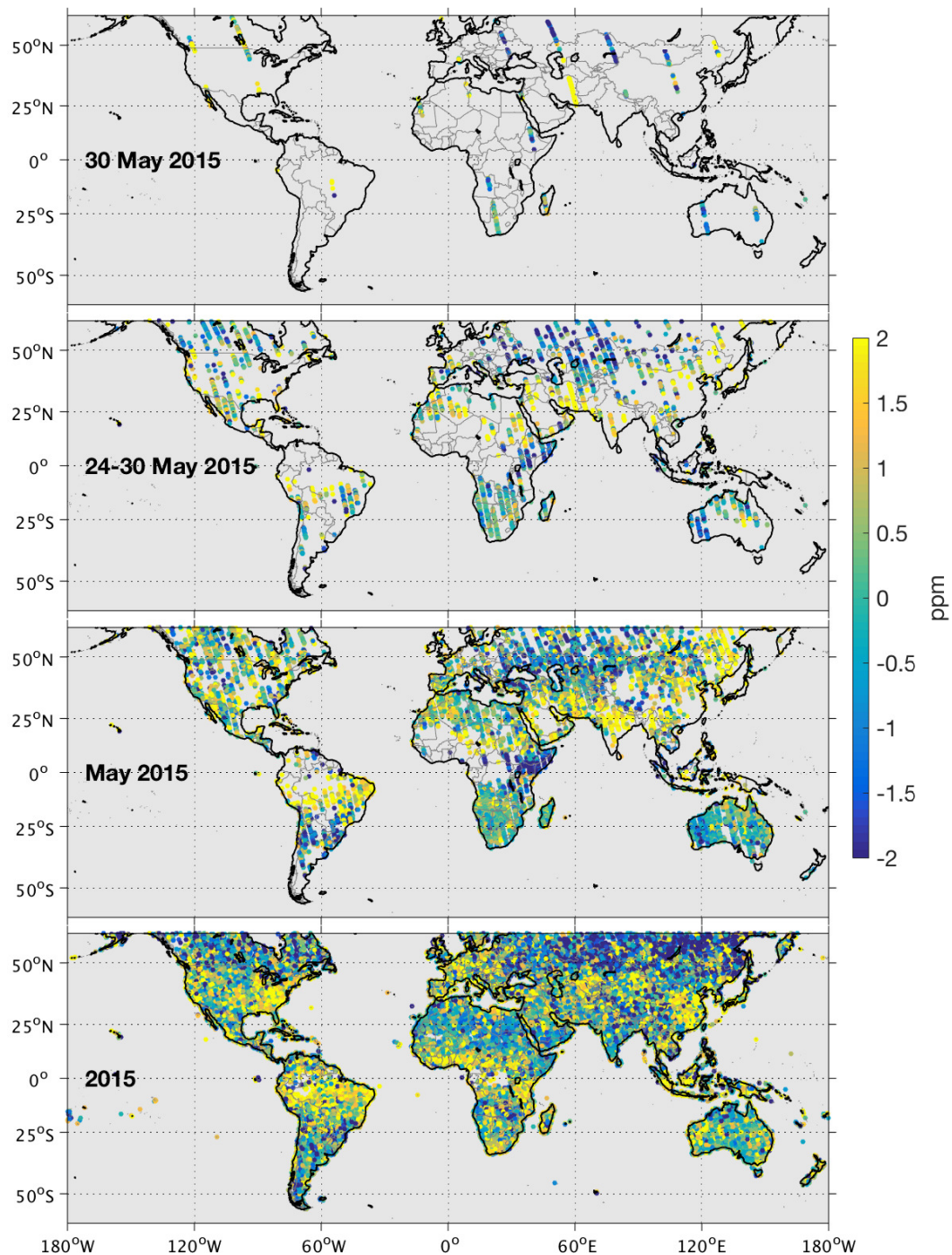


**Figure 1.** Spatial distribution of OCO-2 measurements during one day, one week, one month and one year. The color code indicates the XCO<sub>2</sub> anomalies as derived in Eq. 1. All measurements are illustrated with the same marker size and do not correspond to OCO-2 pixel size.

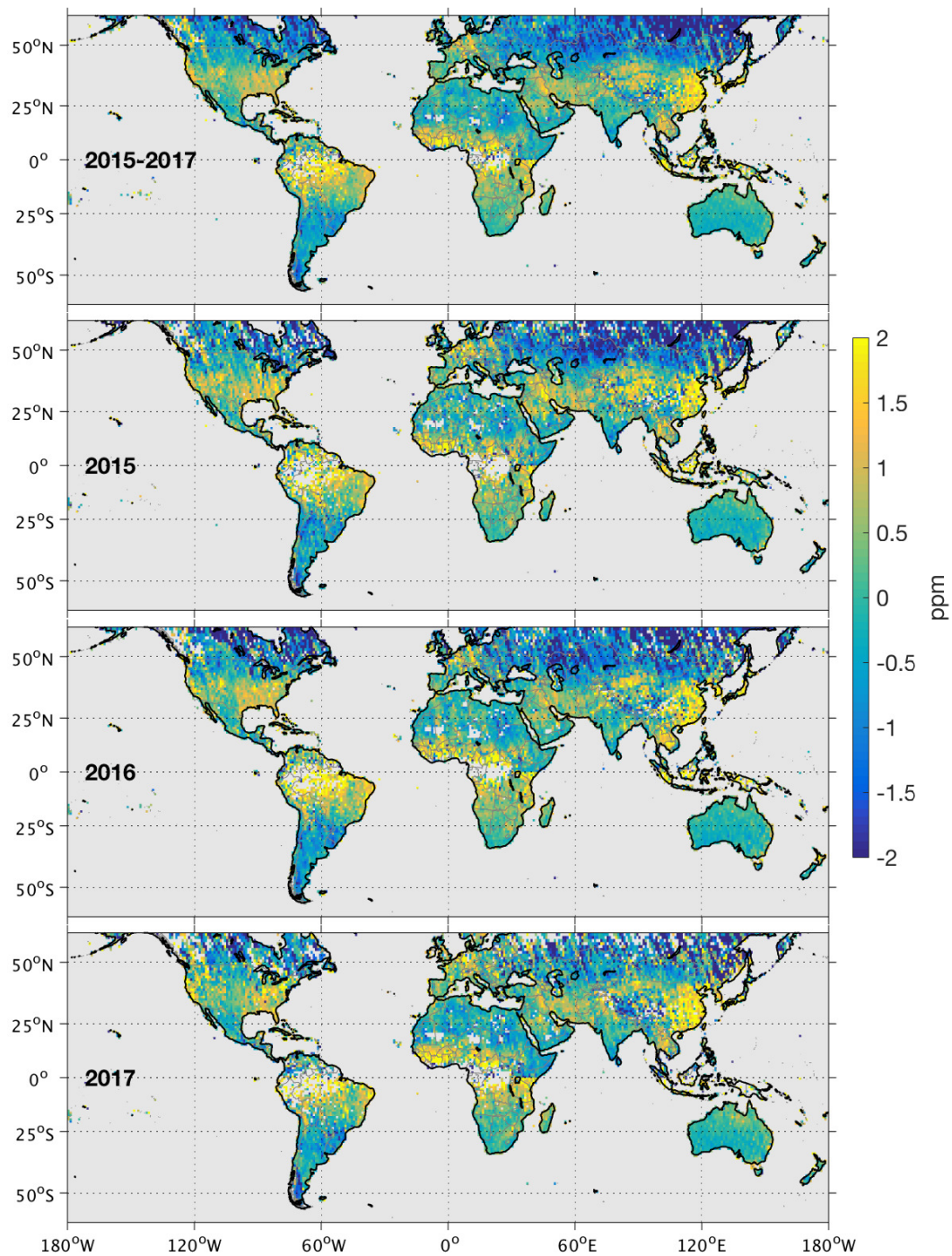


**Figure 2.** Global XCO<sub>2</sub> anomalies as seen by OCO-2. The upper panel corresponds to the three-year average 2015–2017, while the second, third and fourth panels include the annual mean anomalies for 2015, 2016 and 2017, respectively.

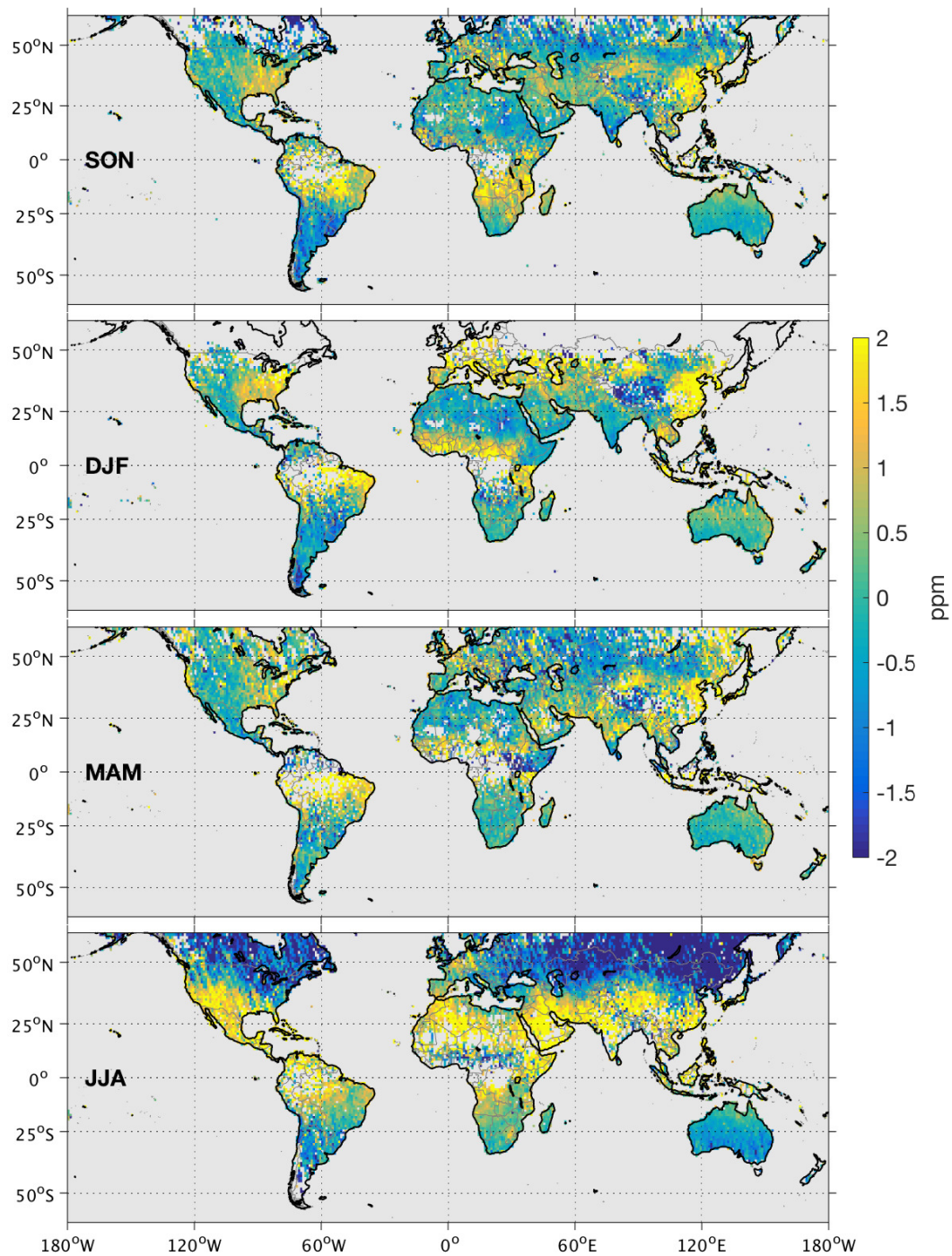


**Figure 3.** Seasonal XCO<sub>2</sub> anomalies 2014–2017 for September–October–November, December–January–February, March–April–May and June–July–August (top to bottom panels, respectively).

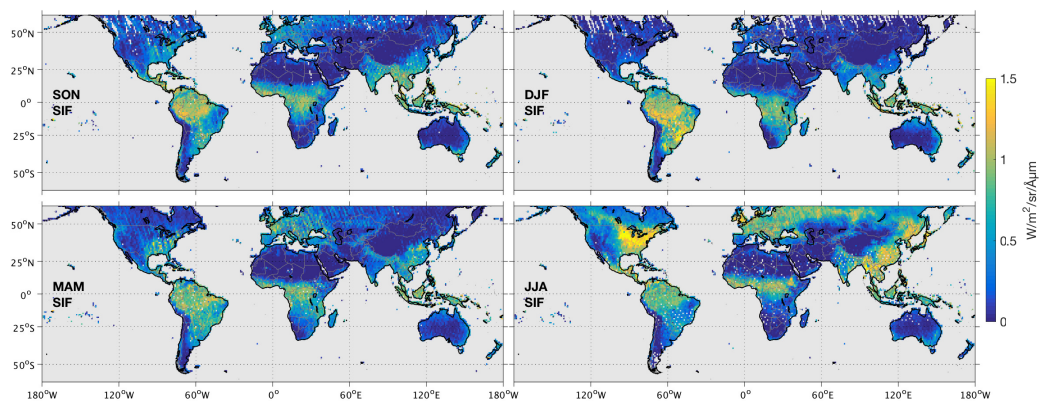


**Figure 4.** Seasonal OCO-2 solar-induced chlorophyll fluorescence (SIF) at 757 nm for different seasons (from September 2014 to August 2015).

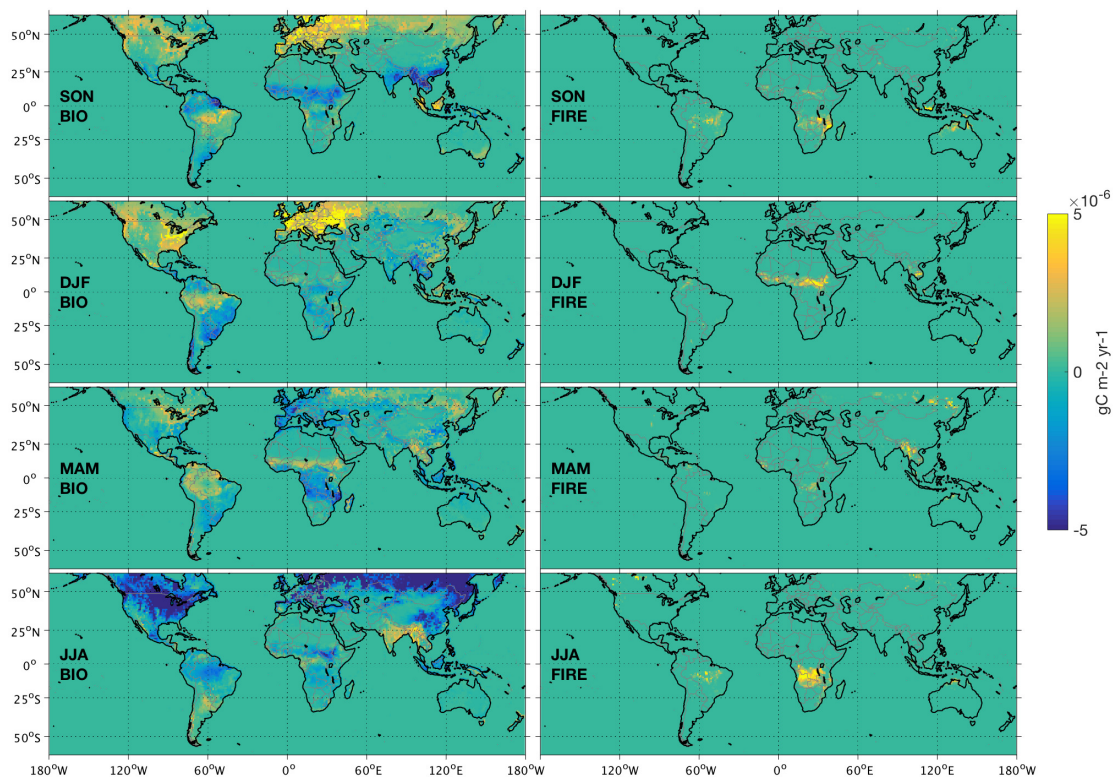


**Figure 5.** Seasonal biospheric (BIO) and biomass burning (FIRE) fluxes from NOAA CarbonTracker from September 2014 to August 2015.

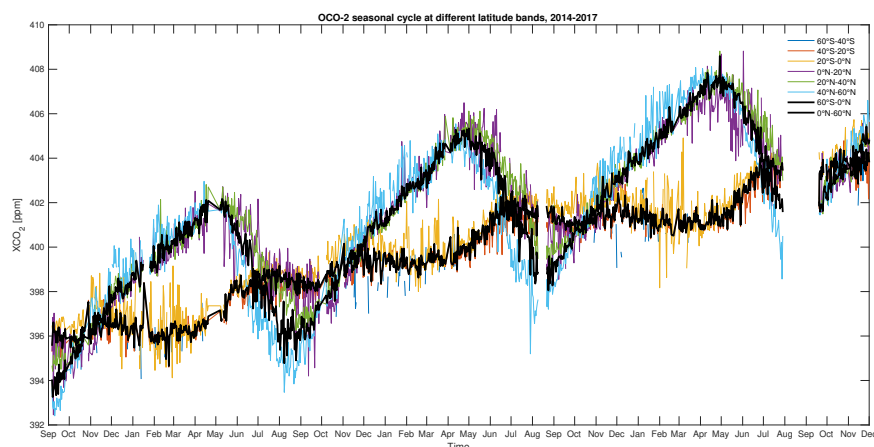


**Figure 6.** XCO<sub>2</sub> seasonal cycle as seen by OCO-2 over different latitude bands.

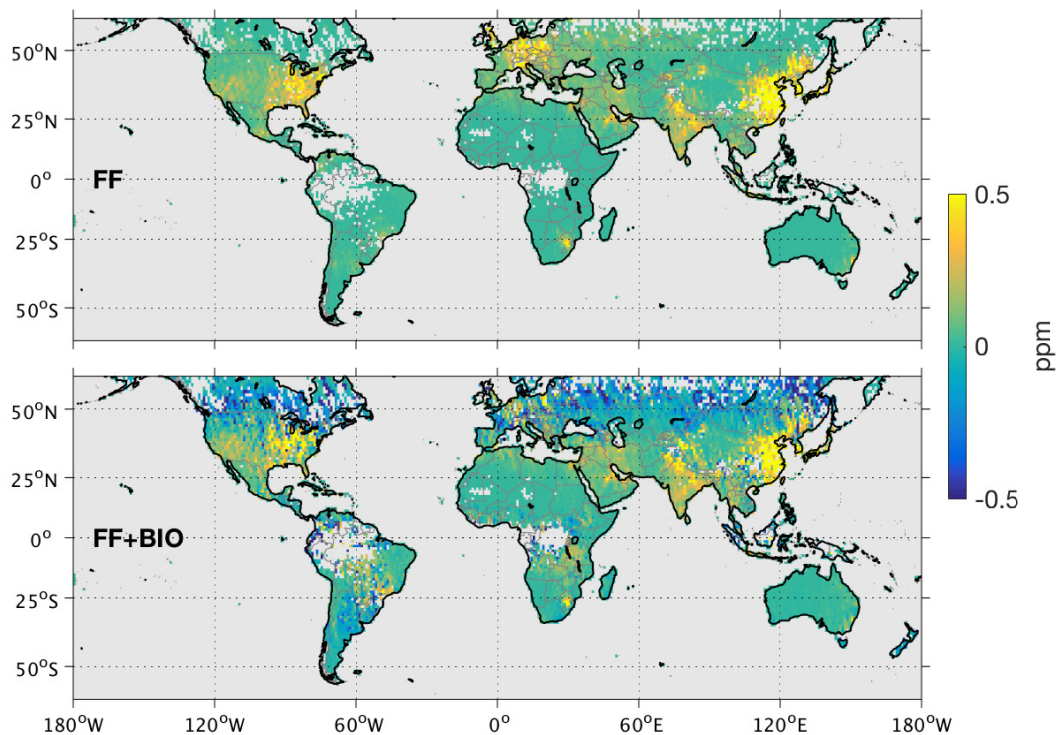


**Figure 7.** FLEXPART simulation results for the year 2015 with contribution from fossil fuel combustion (FF) only and also with biospheric component (FF+Bio). Supplementary material includes also the simulations for year 2016.

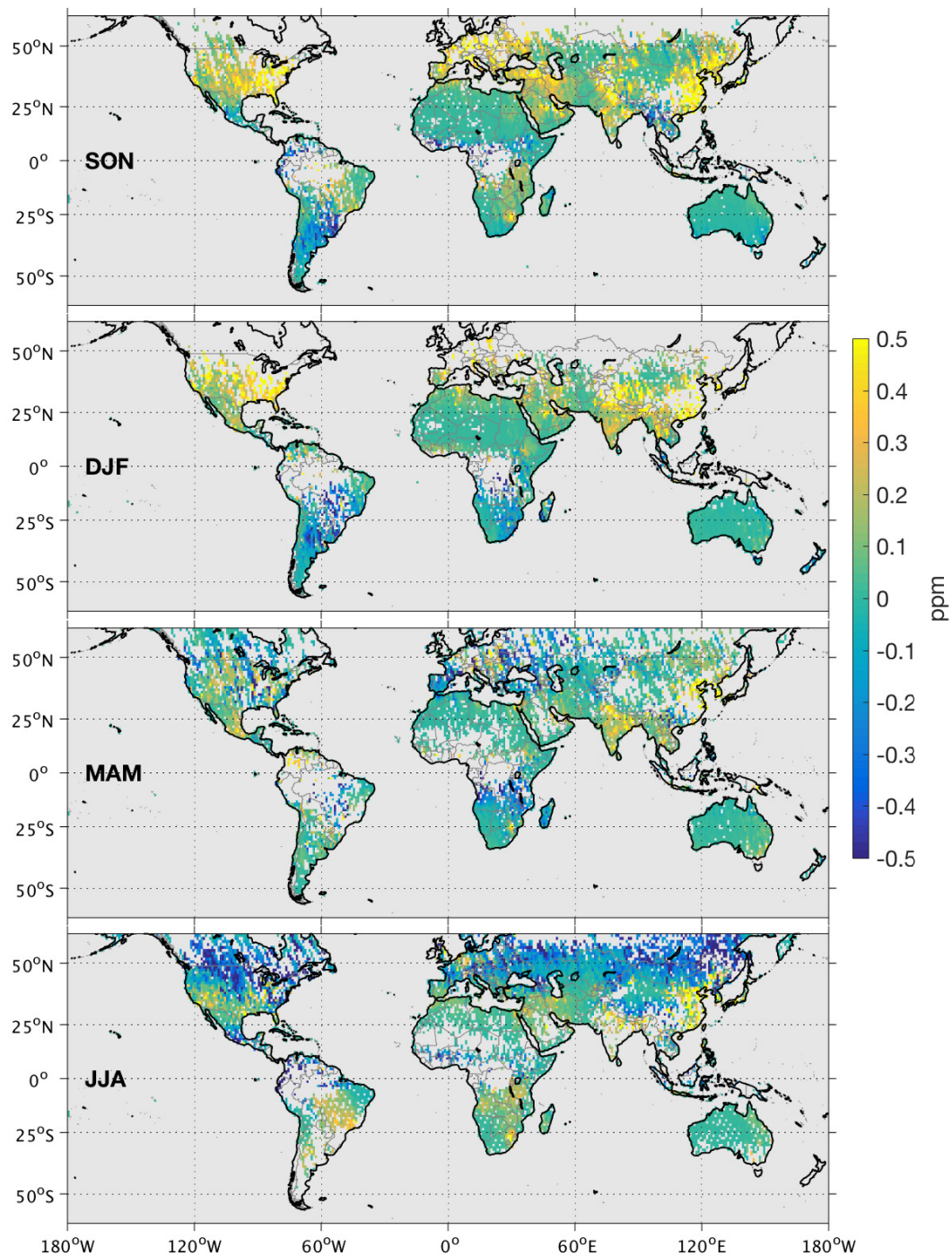


**Figure 8.** FLEXPART seasonal XCO<sub>2</sub> enhancement simulations from September 2014 to August 2015, including fossil fuel and biospheric contribution (FF+BIO).

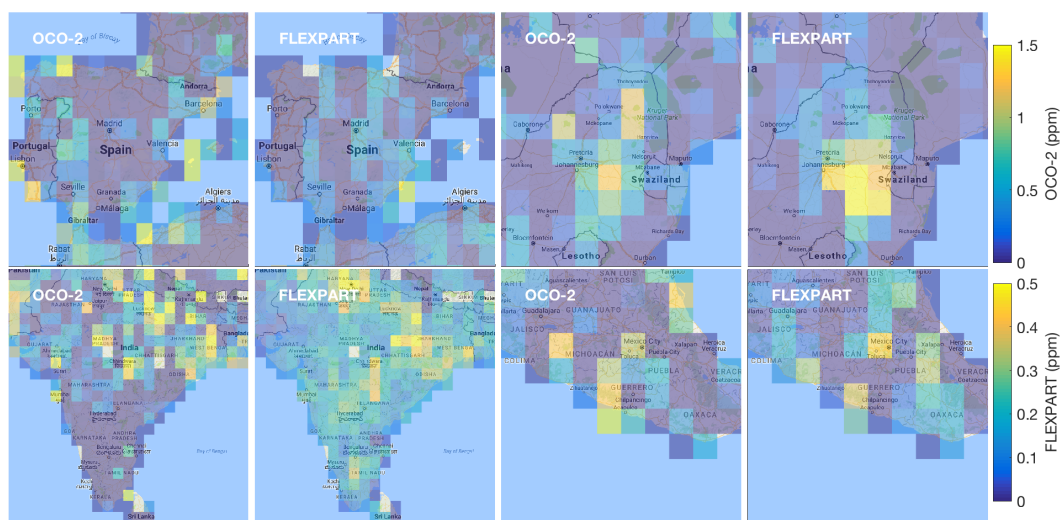


**Figure 9.** Case studies for the year 2015. OCO-2 XCO<sub>2</sub> anomalies and FLEXPART XCO<sub>2</sub> enhancements are overlapped to the Google map background.